Local Structure of Syndiotactic Poly(methyl methacrylate). A Combined Study by Neutron Diffraction with Polarization Analysis and Atomistic Molecular Dynamics Simulations

A.-C. Genix,[†] A. Arbe,[‡] F. Alvarez,[‡,§] J. Colmenero,*[,†,‡,§] W. Schweika,[⊥] and D. Richter[⊥]

Donostia International Physics Center, Paseo Manuel de Lardizabal 4, 20018 San Sebastián, Spain;
Unidad Física de Materiales (CSIC-UPV/EHU), Apartado 1072, 20080 San Sebastián, Spain;
Departamento de Física de Materiales (UPV/EHU), Apartado 1072, 20080 San Sebastián, Spain; and
Institut für Festkörperforschung, Forschungszentrum Jülich GmbH, D-52425 Jülich, Germany

Received February 20, 2006; Revised Manuscript Received March 27, 2006

ABSTRACT: The local structure of syndiotactic poly(methyl methacrylate) (PMMA) has been investigated by combining neutron scattering and fully atomistic molecular dynamics simulations. Selectively deuterating parts of the PMMA monomer, we have accessed five different partial structure factors in the glassy state by neutrons, and polarization analysis has allowed isolating the coherent contribution to the total scattering. In addition, the temperature dependence of the static structure factor has been determined on the fully deuterated sample. The different measured partial structure factors show qualitatively different features with respect to peak positions and heights and provide a very critical check to validate the simulated structure. To gain deep insight into the structure, we have grouped the simulation results in terms of three molecular substructures: the main chain, the α-methyl group, and the ester side group. The study of the resulting partial structure functions has revealed the origin of the diffraction peaks, including those in the X-rays pattern reported in the literature. In addition, a real-space evaluation of the characteristic radial distribution functions has allowed separating intra- and interchain contributions to the total correlation functions. We have found that (i) PMMA exhibits a strong local order with an average main-chain distance of ≈8.6 Å, (ii) this is the only average interchain distance and thus no precursor effect of a layered structure is found, (iii) the main chain shows a persisting all-trans structure, and (iv) a strong anticorrelation between the main chain and the ester side groups, together with an interdigitation of the side groups, suggests a marked separation between the backbone and the side-group spatial arrangements.

I. Introduction

During past years a significant effort has been devoted to unravel the short-range order in polymer melts. Certainly, a better knowledge of the structural features in complex glass-forming systems is an essential key also to understand their dynamical behavior. In particular, special interest has been attracted by the poly(*n*-alkyl methacrylate) (P-*n*MA) series, as it exhibits a strong tendency for local ordering in parallel to an unusual dynamics at the glass transition: Two distinct relaxation processes, each displaying typical characteristics of a dynamic glass transition, are reported for the higher members of the series (see, e.g., refs 1−5 and references therein). This astonishing feature in homopolymers reminds of hairy rods systems and can be attributed to the P-*n*MA's chain structure which is made of two incompatible parts, i.e., flexible alkyl pendant groups attached to a less flexible and polar backbone. As reviewed by Beiner,[2] this situation may lead to a nanoscale phase separation displaying alkyl nanodomains.

In diffraction experiments on polymers, the effects of short-range order are apparent for Q values higher than about 0.5 $Å^{-1}$ (Q: scattering vector). The P-*n*MA's have been extensively studied by using wide-angle X-ray scattering (WAXS).[1,3,6−9] In the Q range between 0.5 and about 2 $Å^{-1}$, the WAXS curves exhibit three scattering peaks for P-*n*MA's containing from 2 to 12 carbon atoms in the alkyl groups. The first peak (I) is located at $Q \approx 1.3$ $Å^{-1}$, and it is interpreted as the mean van der Waals distance between nonbonded atoms in the amorphous polymer. A second peak (II) is found at $Q \approx 0.8$ $Å^{-1}$ and is not easily distinguishable in the higher P-*n*MA's,[6] if it is there at all. In both cases, the positions of the maxima are independent of the length of the side chains. In contrast, the position of the third peak at lower Q's (III) depends on the alkyl group length. In a Bragg approximation, the repeating distance in real space is given by $d = 2\pi/Q_{\max}$. For peak III, the relationship between d_{III} and the number of alkyl carbons in the side group, N, may be expressed in two different ways. The first model[7,10] is a two-dimensional idealized picture leading to a formulation $d_{\mathrm{III}} = d_0 + aN$, where d_0 corresponds to the effective diameter of the main chain including the carboxyl group and a is an average increment per each CH_2 unit in the side chain. In this representation, d_{III} is related to the typical distance between main chains separated by side chains in a close to all-trans conformation. The second scenario considers that the alkyl side chains form Gaussian random coils and consequently proposes a nonlinear increase[6] of d_{III} with N as $d_{\mathrm{III}} = d_0 + aN^{1/2}$. In this case, the equivalent Bragg spacing is associated with the distance between closest alkyl side-chain domains in the melt. This last picture would be more realistic in the case of long alkyl chains, whereas the first model is more consistent with short alkyl chains.[2] Finally, looking to a global structure in the P-*n*MA series, Wind et al.[8] recently proposed an extension to the model of Arrighi et al.[10] with a main-chain arrangement in the third dimension. This correlation would be related to peak I, and the corresponding distance is visualized as the intermolecular spacing between two adjacent main-chain segments ($d_{\mathrm{I}} \approx 5$ Å).[8] In addition, the authors assigned the position of peak II ($d_{\mathrm{II}} \approx 8$ Å) to the intrasegmental distance between closest side groups

---

[†] Donostia International Physics Center.
[‡] CSIC-UPV/EHU.
[§] UPV/EHU.
[⊥] Forschungszentrum Jülich GmbH.
* Corresponding author. E-mail: wapcolej@sc.ehu.es.

10.1021/ma060370t CCC: $33.50

on the same side of the polymer chain. In the proposed scenario, the nanophase separation tendency between incompatible alkyl groups and polar backbones would lead to a layered structure with the main chains stabilized in an extended conformation that forms sheets separated by side-chain layers.

Among this trend reported for the P-*n*MA series, the X-ray scattering pattern of poly(methyl methacrylate) (PMMA) in the Q range between 0.5 and 2 $Å^{-1}$ presents a clearly anomalous behavior with a single scattering peak at $Q \approx 1$ $Å^{-1}$, i.e., between the previously discussed peak I and peak II.[6,7,9,11] This peak appears quite symmetrical with no indication of any unresolved contribution.[7] As commented by Wind et al.,[8] the absence of peak III in PMMA seems reasonable as already for PEMA ($N = 2$) the contribution of peak III to the WAXS pattern is very weak (due to the short size of the side groups that cannot act together). However, the authors could not explain why the high conformational ordering of the ester groups[9] and the packing of the main chains are not detected in the corresponding WAXS curve. By using the scattering from an oriented sample, Lovell and Windle[9] showed that the main peak in PMMA contains a dominant intermolecular contribution at $Q = 0.95$ $Å^{-1}$ with a small intramolecular component at $Q = 1.2$ $Å^{-1}$. Looking at higher Q, they established that the two additional scattering peaks at $Q = 2.2$ and 3 $Å^{-1}$ are related to periodicities along the polymer chains. From that work, the authors derived a precise local conformation structure that is in very good agreement with previous energy calculations from Sundarajan and Flory;[12] i.e., PMMA would display a curved structure—due to large bond angles at CH_2 that minimize steric interactions—in a nearly all-trans conformation.

Thus, the following key question still remains open: is the tendency for local ordering reported in the P-*n*MA series also present in its shortest homologue? With these ideas in mind, in this work we have focused on syndiotactic PMMA in order to further investigate the local structure of this intriguing polymer. As mentioned, X-ray studies have already been reported on this system (see, e.g., refs 6, 7, 9). However, taking into account the complexity of the polymer, the information provided by this technique—essentially highlighting the partial structure factors involving carbons and oxygens—is rather limited and does not allow to unveil the short-range order details. Additional and complementary experimental information on particular correlations arising from different groups of selected atoms can be achieved by the study of other partial static structure factors. These can be accessed by using neutron diffraction combined with isotopic substitution techniques. The very different neutron scattering lengths of hydrogen and deuteron atoms allows selectively highlighting certain atomic pair correlations. Moreover, with the help of polarization analysis of the diffracted neutrons, the coherent contribution to the scattering can be determined at an absolute scale. In our study we have considered five possible deuteration labelings of PMMA. Thus, from an experimental point of view, this work constitutes the largest effort ever done to study the local structural properties of syndiotactic PMMA. However, and unfortunately, the interpretation of the experimental results in terms of the atomic correlations is usually extremely difficult. Therefore, we have combined our neutron diffraction results with fully atomistic molecular dynamics (MD) simulations. This approach has proven to be highly successful to decipher the short-range order and its relation to the particular microstructure in several glass-forming polymers.[13−18] Simulation enables precise insight into the atomic structure and allows calculating magnitudes that cannot be experimentally accessed. However, fully atomistic and realistic samples are necessary. Therefore, a first thorough validation step is mandatory by comparison with experimental data. The most critical check of the structural resembling of the simulated cell and the real system is achieved by comparing the largest possible number of partial structure factors—just in the way done in this work.

After ensuring the reliability of the simulation we have exploited its capabilities. By using a suitable grouping of the 45 partial correlation functions based on specific molecular groups in the repeat unit, we have unveiled the origin of the correlations contributing to the diffraction peaks and produced new insights into the structural peculiarities of this polymer. Moreover, we have also scrutinized the radial distribution functions in real space and separated their inter- and intramolecular contributions. This information is also of great interest in order to understand the dynamical behavior (see, e.g., ref 19). Experimentally, from phenomenological studies like e.g., following the temperature dependence of the diffraction maxima, it is possible to qualitatively assign a predominantly inter- or intramolecular character to the different peaks.[20] However, a proper disentanglement of these contributions can only be performed with the help of MD simulations. This has been done in relatively simple polymers like, e.g., polybutadiene[21,22] and also in other chemically more complex systems like, e.g., polycarbonate[23] and polystyrene.[24,25]

The paper is organized as follows. After the experimental details and the simulation method (sections II and III), the results are presented in section IV, demonstrating the validation of the simulations. The discussion (section V) is divided into four parts. The first concentrates on the molecular based partial structure factors contributing to the total static structure factor of PMMA, whereas the second part relates to the experimental partial structure factors weighted by the proper scattering lengths. Thereafter, the radial distribution functions in real space are studied for selected pairs of atoms, addressing the inter- and intrachain character of the contributions (section V.C). Closing the discussion, we present a comparison with literature results on PMMA and the P-*n*MA series.

II. Experimental Section

A. Samples. Five PMMA samples (Polymer Source, Inc.) with different deuteration levels were investigated: fully protonated (PMMA-h8), fully deuterated (PMMA-d8), protonated with deuterated α-methyl groups (PMMA-d3α), protonated with deuterated ester methyl groups (PMMA-d3e), and deuterated with protonated ester methyl groups (PMMA-d5) (Figure 1 shows the monomeric unit of PMMA in the right down corner). The molecular weights and polydispersities are given in Table 1. The glass-transition temperatures determined by DSC were $T_g \approx 400$ K. The tacticity of the polymers was close to 80% syndiotactic.

B. Neutron Diffraction. Neutron diffraction assesses the differential cross section, i.e., the number of scattered neutrons into a solid angle between Ω and $\Omega + d\Omega$, relative to the number of incident neutrons.[26,27] The modulus of the momentum transfer, Q, is determined by $Q = 4\pi \sin(\theta/2)/\lambda$, where θ is the scattering angle and λ the wavelength of the incoming neutrons. The differential cross section contains scattering of two natures: coherent and incoherent. The coherent contribution can be expressed as

$$\left(\frac{\partial\sigma}{\partial\Omega}\right)_{\mathrm{coh}} = \frac{1}{N}\langle\sum_{i,j=1}^{N}\bar{b}_i\bar{b}_j e^{i\vec{Q}\vec{r}_{ij}}\rangle \qquad (1)$$

where the $\bar{b}_i$ stand for the coherent scattering lengths for neutrons (see Table 2) and N is the number of atoms. $\vec{r}_{ij} = \vec{r}_i - \vec{r}_j$ is the vector connecting atoms i and j at the same time, and the brackets denote the thermal average. The $Q \to \infty$ limit of the coherent

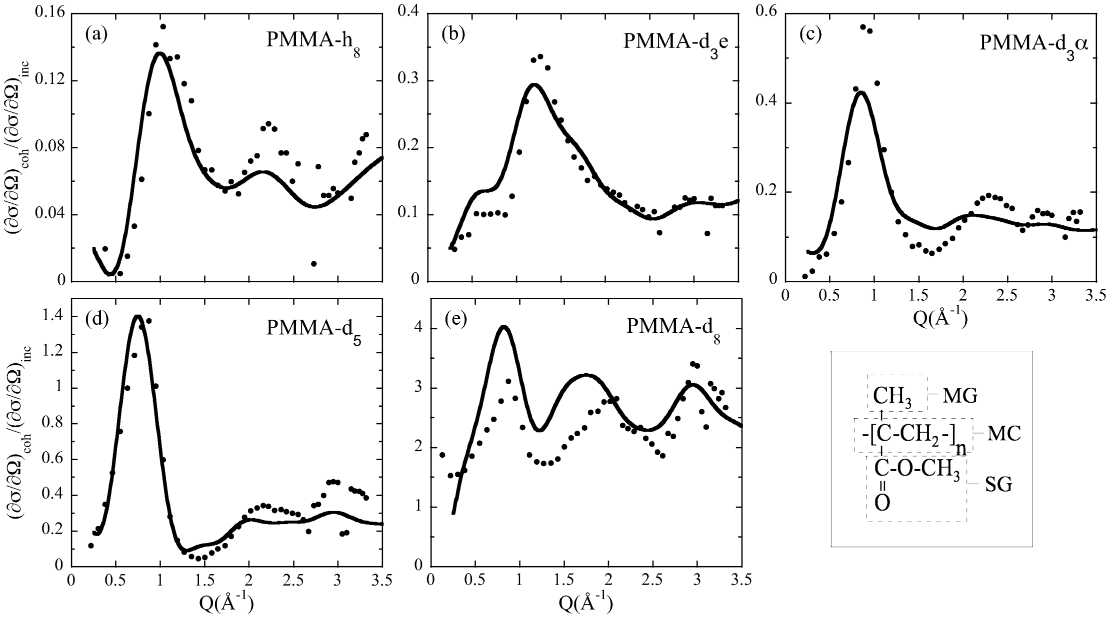

Figure 1. Ratio between the coherent and the incoherent differential cross sections measured by DNS at 300 K (dots) or calculated from the MD simulations at 580 K (lines) for the different samples investigated. The chemical formula of PMMA showing the different molecular groups considered in the analysis is also displayed.

Table 1. Molecular Weight, Polydispersity, and Coherent and Incoherent Cross Sections of the Samples Investigated

sample	M_w	M_w/M_n	σ_{coh}(barn/ monomer)	σ_{inc}(barn/ monomer)
PMMA-h8	27 500	1.1	50.27	642.09
PMMA-d8	26 800	1.04	80.95[a]	16.41[a]
PMMA-d3α	25 300	1.09	61.78	407.46
PMMA-d3e	25 000	1.04	61.78	407.46
PMMA-d5	29 000	1.04	69.45	251.04

[a] Assuming full deuteration.

Table 2. Coherent Scattering Lengths and Coherent and Incoherent Cross Sections for Neutrons of the Nuclei Composing the Samples

nucleus	$\bar{b}$ (fm)	σ_{coh} (barn/atom)	σ_{inc} (barn/atom)
H	−3.7406	1.7583	80.27
D	6.671	5.592	2.05
C	6.6511	5.559	0
O	5.803	4.232	0

differential cross section is determined by the coherent cross section σ_{coh}:

$$\lim_{Q\to\infty}\left(\frac{\partial\sigma}{\partial\Omega}\right)_{coh}=\frac{1}{N}\sum_{i=1}^{N}\bar{b}_i^{\,2}=\frac{\sigma_{coh}}{4\pi} \tag{2}$$

The cross sections like σ_{coh} are given in units of barn/scattering unit, and $(\partial\sigma/\partial\Omega)_{coh}$ is in units of barn/(sr scattering unit) (1 barn $= 10^{-28}$ m^2). On the other hand, in an ideal case, the incoherent contribution to the differential cross section is Q-independent and given by the total incoherent cross section σ_{inc}:

$$\left(\frac{\partial\sigma}{\partial\Omega}\right)_{inc}=\frac{1}{4\pi N}\sum_{i=1}^{N}\sigma_{inc}^{i}=\frac{\sigma_{inc}}{4\pi} \tag{3}$$

(see Table 2). The values of the coherent and incoherent cross sections of the samples investigated can be found in Table 1.

From Tables 1 and 2 we can deduce that the scattering from a fully deuterated sample like PMMA-d8 is predominantly coherent and reveals to a very good approximation the structure factor $S(Q)$, since the scattering lengths for all the atoms involved are very similar. Furthermore, fully protonated samples like PMMA-h8 scatter most of the neutrons incoherently, and in this case the weak coherent scattering reveals a partial structure factor rather similar to that observed by X-rays—for both probes, neutrons and X-rays, carbon and oxygen show much bigger scattering lengths than hydrogens. The case of the partially deuterated samples is in between and delivers additional independent information on other partial structure factors.

Standard diffractometers access the total diffential cross section, including both coherent and incoherent contributions. However, there is the possibility of experimentally separating these contributions to the scattering by using a spin-polarized neutron beam and polarization analysis (see, e.g., refs 26 and 27). This is due to the fact that if the incoherent scattering arises solely from spin disorder, it flips the neutron spin with probability 2/3, while coherent scattering leaves the spin unchanged. Thus, with the incident beam polarized, the number of neutrons scattered within a given solid angle with spin flipped (SF) and nonspin flipped (NSF) is

$$I_{SF}=I_0\frac{2}{3}\left(\frac{\partial\sigma}{\partial\Omega}\right)_{inc} \tag{4}$$

$$I_{NSF}=I_0\left[\left(\frac{\partial\sigma}{\partial\Omega}\right)_{coh}+\frac{1}{3}\left(\frac{\partial\sigma}{\partial\Omega}\right)_{inc}\right] \tag{5}$$

where I_0 is a proportionality factor that depends on the experimental conditions (amount of sample in the beam, primary beam intensity, detector efficiencies, etc.). In the absence of inelasticity and multiple scattering, the value of I_0 can easily be obtained from the SF measurement and the simple calculation of σ_{inc}; then, the partial structure factor can be determined in a straightforward way from the NSF measurement in absolute units.

1. DNS Measurements. Based on this principle, in this work we used the diffuse scattering spectrometer DNS[28] at the FZ Jülich (Germany), in its diffraction mode. This instrument is equipped with a horizontally and vertically focusing monochromator, and a wide angular range around the sample is covered with detectors. Incident neutrons can be polarized by a focusing bender assembled by a stack of supermirrors. A detector bench with 12 detector units is equipped with similar benders for polarization analysis. For spin-flip measurements a Mezei-type flipper is installed in the incident beam. The incident wavelength was set to 3.3 Å, enabling a range of scattering vectors Q up to 3.34 Å^{-1}. The experiments were performed at 300 K for all samples. These were put as films into hollow cylindrical aluminum sample holders of 10 mm diameter. The thicknesses were such that a transmission of ≈90% was expected in all cases. The correction for background scattering was done by the measurement of the scattering from the empty cell. The corrections for multiple scattering have been done in a similar way to ref 16.

2. D20 Measurements. The temperature dependence of the static structure factor was investigated on the fully deuterated sample by D20 at the Institut Laue-Langevin (ILL, Grenoble, France). D20 is a high-flux, medium-resolution powder diffractometer equipped with a large-area linear curved position-sensitive detector. This diffractometer has no option to separate coherent and incoherent scattering. With $\lambda = 1.3$ Å a range of scattering vectors up to 9 Å^{-1} was covered. The sample was filling a cylindrical vanadium sample holder of 6 mm diameter. The advantage of vanadium is that it does not show any Bragg peak over the large Q range investigated. The temperatures investigated were 300, 400, and 500 K. The data were corrected for detector efficiency using a vanadium standard and for background scattering by empty cell measurements.

III. Simulation Method

The molecular dynamics simulations were carried out by using the Insight (Insight II 4.0.0 P version) and the Discover-3 module from Molecular Simulations Inc. (now Accelrys) with the Polymer Consortium Force Field (PCFF) (detailed information can be found in refs 29−31). The model system was built by means of the well-known amorphous cell protocol.[32,33] In this work, a cubic cell containing four identical polymer chains of 25 monomer units each of PMMA with a tacticity degree close to 80% syndiotactic was constructed at 580 K with a density fixed to be unity. Periodic boundary conditions were assumed to model the bulk system. Standard minimization procedures (Polak−Ribiere conjugate gradients method) were applied to the constructed sample in order to minimize the so-obtained energy structure, and a subsequent dynamics was run for 20 ns at 580 K in order to equilibrate the sample. The chosen temperature is high enough to allow local structural equilibration of the sample in this time. To get an estimation of the density value, a 1 ns run under NPT conditions was carried out; i.e., the value of the pressure was fixed (chosen to be the atmospheric one $P = 0.0001$ GPa), and the cell size was allowed to rearrange to the new conditions (that is, letting the density rearrange, since the number of atoms, N, is constant). All this was done by means of the Berendsen procedure. In the corresponding output file, we chose one cell following two criteria: a density close to the average density over the complete NPT run ($\langle\rho\rangle = 1.0448$ g/cm^3) and a corresponding pressure value close to the atmospheric pressure. By this way, the selected cell corresponds to a density of 1.0445 g/cm^3 with a cell dimension of 25.16 Å of side. The following simulations were carried out at 580 K in the NVT ensemble—where the cell size and the temperature of the sample are constant—together with the velocity scaling (temperature window of 10 K) for temperature control.[34,35] As an integration method we have used the velocity-Verlet algorithm with a time step of 1 fs. During the first 1 ns run the new cell was still allowed to equilibrate. Afterward, a 1 ns run was launched, collecting data every 0.01 ps. Two more successive runs of 2 and 20 ns were carried out, collecting data every 0.05 and 0.5 ps, respectively. Nearly indistinguishable results were obtained from the different simulation runs. Thus, no signature of any aging process was observed during the successive runs, confirming local equilibration of the sample.

From the atomic trajectories in real space it is possible to follow separately the different atomic correlations in the sample cell. For instance, the partial radial distribution functions $g_{\alpha\beta}(r)$ can be calculated. These are defined as

$$g_{\alpha\beta}(r) = \left\langle \frac{1}{N} \sum_{i\alpha,j\beta}^{N_\alpha N_\beta} \delta[\vec{r} - (\vec{r}_{i\alpha} - \vec{r}_{j\beta})] \right\rangle \tag{6}$$

where the labels α and β refer to specific kinds of atoms (e.g., main-chain carbons, α-methyl group hydrogens, etc.). The sum runs over all the different atoms of kinds α and β [there N_α (N_β) are the total number of atoms of kind α (β)]. The positions of the atoms in eq 6 are considered at the same time, and the average is performed for a large number of frames throughout the atomic trajectories.

The direct comparison with the experimentally accessed cross sections in Q-space can be realized by computing the Fourier transform of $g_{\alpha\beta}(r)$, $a_{\alpha\beta}(Q)$. The coherent cross section measured by neutron scattering can thus be obtained as

$$\left(\frac{\partial\sigma}{\partial\Omega}\right)_{\text{coh}} = \sum_{\alpha\beta} \bar{b}_\alpha \bar{b}_\beta a_{\alpha\beta}(Q) \tag{7}$$

where all the atomic species distinguished in the sample are considered and weigthed by the corresponding scattering length of the involved isotopes.

IV. Results

The symbols in Figure 1 display the experimental results obtained by DNS for the five samples investigated at 300 K. As can be appreciated in this figure, the different partial structure factors revealed by the different deuteration labels reflect the complexity of the short-range order in this polymer. The main peak appears at different positions depending on the partial structure factor considered. Furthermore, we note that the neutron diffraction pattern for the PMMA-h8 sample looks rather close to that obtained from X-rays measurements.[6−9] As already mentioned, this is due to the similar weighting of the atomic correlations for X-rays and neutrons in protonated samples. However, (i) the oxygen contributions have a significantly higher weight in the case of X-rays, (ii) CH$_2$ groups do not contribute much in the case of neutrons, and (iii) X-rays scattering factors are Q-dependent. On the other hand, we note that in the case of PMMA-d8 the DNS data reveal that the deuteration is not completely perfect. As can be deduced from Table 1, the high-Q limit for the ratio between coherent and incoherent scattering in this sample should be of 4.9. The experimental data are clearly below this limit, indicating an extra incoherent contribution from remaining hydrogens in the sample.

The DNS results in Figure 1 are compared with their counterparts obtained from the MD simulations at 580 K (lines). For the PMMA-d8 sample, in the calculations we have assumed a deuteration level of 98%, which allows matching the experimental data in the high-Q region accessed by DNS. Though both series of data do not perfectly coincide, we emphasize that the global behavior is very well reproduced by the simulations. Thereby, we have to take into account that the comparison is extended beyond the structure factor accessed by X-rays, which is the only function usually considered. Moreover, we have also to consider that the existing slight discrepancies might relate to the difference in temperature that is rather big. There are several reasons preventing the comparison of simulations and experiments at the same temperature. First, from the side of the simulations, reasonably equilibrated samples below the glass transition that could be directly compared to the DNS data cannot be achieved. From an experimental point of view, diffraction experiments at high temperatures are seriously hampered by inelasticity effects, which become very strong above the glass-transition temperature. This can be observed from Figure 2, where the D20 diffraction patterns from the PMMA-d8 sample are shown for 300, 400 ($\approx T_g$), and 500 K. This figure reveals that the high atomic mobility in the supercooled liquid state leads to a strong decay of the measured intensity, mainly at high Q. This effect is very difficult to correct, and the usual Placzek corrections[36,37] do not properly work with light atoms.[16] What is important to realize from Figure 2 is the general effect of temperature on the structure factor that can be deduced from the evolution of the experimental data between 300 and 400 K, where inelasticity effects are much less evident: (i) the peak at $Q \approx 3$ Å^{-1} is not affected by temperature; (ii) the peak at $Q \approx 2$ Å^{-1} is also unaffected in its high-Q flank; (iii) the main differences appear below 2 Å^{-1}. While the high-Q result reflects correlations based on covalent bonds, obviously the lower Q/larger distance correlations contain significant contributions from noncovalently bonded atoms. There, we observe in detail that the minimum between the two first peaks becomes less pronounced and that the intensity of the first peak increases in its low-Q flank and in the region of the maximum (see the inset). In a qualitative way, these are also the differences observed between the simulations results at 580 K and the DNS results at 300 K (see Figure 1e). This similar tendency supports the assumption that the discrepancies noticed in the detailed comparison of both sets of data are related to the difference in temperature.

Thus, we can conclude that the structural features of the simulated PMMA sample are a fair representation of those characteristic for the real polymer. This allows us to go beyond the simple validation of the simulations and calculate magnitudes that are not experimentally accessible and reveal in detail the origin of the short-range order in PMMA.

V. Discussion

A. Molecular-Based Partial Structure Factors. The monomer unit of PMMA is built from 15 atoms with 9 of them nonequivalent. This leads to 45 different partial correlation functions $g_{\alpha\beta}(r)$ or, in Q space, $a_{\alpha\beta}(Q)$. Looking on all of them in detail separately is not very meaningful. To get insight, it is far better to group them according to the molecular composition of the PMMA monomer (see Figure 1). Thus, we will distinguish three different groups: first, the main chain (MC), then the ester side group (SG), and finally the α-methyl group (MG). With this grouping we have three partial correlation functions involving correlations among the atoms belonging to groups of the same kind, namely MC/MC (the term of the main chain), SG/SG (that of the ester side group), and finally MG/MG (describing the term of the α-methyl group). Furthermore, there are three interference terms to consider, relating the three main groups with each other. To show how these molecular-based partial structure factors, $A_{G/G'}(Q)$ (G,G′: MC, MG, SG), are calculated, we consider the cases of the MC/MC and MC/MG correlation functions ($A_{MC/MC}$ and $A_{MC/MG}$). We have

$$A_{MC/MC}(Q) = a_{C_{MC}C_{MC}}(Q) + a_{H_{MC}H_{MC}}(Q) + a_{C_{MC}H_{MC}}(Q) \quad (8)$$

and

$$A_{MC/MG}(Q) = a_{C_{MC}C_{MG}}(Q) + a_{C_{MC}H_{MG}}(Q) + a_{H_{MC}H_{MG}}(Q) + a_{H_{MC}C_{MG}}(Q) \quad (9)$$

Figure 3 displays the six partial correlation functions together with their sum. Here, all atoms are weighted equally, thus presenting the true structure factors. These structure factors are normalized such that in the limit of large Q the terms MC/MC, MG/MG, and SG/SG assume the value of the relative fractions of atoms which are comprised in the corresponding structure factor. For example, the MC/MC structure factor is normalized to the number of carbons and hydrogens in the main chain (408) relative to the total number of atoms in the chain (1508). This gives a value 0.27 to be assumed at high Q. In this way the total structure factor is normalized to 1. Naturally, the cross terms tend to vanish at high Q.

From this grouping, a big deal of important structural information may be obtained. The inspection of the different partial structure factors reveals the following features:

MC/MC: The main chain/main chain correlation function exhibits a very well developed strong peak at $Q = 0.73$ Å^{-1}. Using the Bragg approximation $d_{MC/MC} = 2\pi/Q_{max}$, we can estimate an average distance between the main chains of 8.6 Å. For this peak we note that the amplitude of 1.7 is about 6.3 times higher than the asymptotic limit of 0.27, suggesting strong local ordering. Beyond this main peak the MC/MC structure factor displays a weaker shoulder around $Q = 1.3$ Å^{-1}. The Bragg law gives for this shoulder a characteristic distance of 4.8 Å, which, as we will discuss in section 5.3, relates to intrachain correlations.

MC/SG: The most salient feature of the partial structure factors is the very strong anticorrelation between the main chain and the ester side group. The MC/SG correlation function nearly mirrors negatively the MC/MC partial structure factor, with respect to both its height and width. This tells us that at the first structure factor peak the MC/MC and the MC/SG correlations are out of phase by a phase angle of $\Phi = \pi$. Obviously, there is a strong tendency of local separation of the side groups and the main chains, which may be understood as a precursor of the nanophase separation reported for higher order P-*n*MA’s.[2,8]

SG/SG: The side group/side group correlation function is characterized by a double peak at $Q = 0.70$ Å^{-1} and $Q = 1.23$ Å^{-1}. The two peaks appear to correspond roughly to the first and second feature of the MC/MC correlation function. We note, however, that the major distances appearing in the SG/SG correlation function cannot easily be mapped on those representative for the main-chain correlations. As it will be substantiated later, these two peaks correspond to a large extent to particular intrachain correlations relating to the syndiotactic nature of the molecular structure.

MG/SG: The α-methyl/ester side group correlation function is again phase shifted by a phase factor $\Phi \approx \pi$ with respect to the MC/MC correlations as well as with respect to the SG/SG correlations. We may state that the α-methyl group is covalently fixed to the main chain without an additional degree of freedom for motion. This neglects the methyl-group rotation creating disorder at very short distances. Thus, the α-methyl group should show a similar behavior as the main chain, and therefore the MG/SG correlations should have a similar character as their MC/SG counterpart. Thus, these correlations again may be understood on the basis of a strong local segregation of the side groups from the main chain.

MC/MG: At low Q this correlation function is in phase with the MC/MC structure factor mirroring the main-chain correlations at a very similar repeat distance. This feature again results from the direct association of the α-methyl group and the main chain. Going to somewhat larger Q this correlation function changes sign and now appears to be anticorrelated to the main chain.

MG/MG: The α-methyl/α-methyl group correlations are relatively unstructured. They give rise to a broad maximum at the point where the MC/MC correlations have their first peak. Clearly, the MG/MG correlation function must show similar features as that of the main chain. But then, instead of falling like the main-chain correlations, they exhibit a broad maximum: obviously, because of the syndiotactic chain structure, there are many distances in between the α-methyl groups starting from interchain and approaching intrachain correlations in going to larger Q's. Furthermore, as we will show in section V.C, some interdigitation between neighboring chains leads to the appearance of intercontributions at comparatively short distances.

Total: The resulting total structure factor $S(Q)$ displays three distinct maxima, where only the first maximum has some relations to the underlying partial structure factors. Its Q-position is close to that of the MC/MC correlations and displays roughly the total periodic structure of the chain arrangements. Interestingly, the second and third peak arrive from a very complicated superposition of trailing partial structure factors and do not correspond to clear maxima or minima of those functions.

B. Experimental Partial Structure Factors. Until now we have discussed the atom-weighted correlation functions $A_{G/G'}(Q)$. Now, Figure 4a−e displays the neutron scattering length weighted partial structure factors, which correspond to the different experimental structure factors as shown in Figure 1. For example, the contribution of the MC/MG correlations to the partial structure factor of PMMA-d3α is

$$\left(\frac{\partial\sigma}{\partial\Omega}\right)_{\text{coh}}^{\text{MC/MG}}(Q) = \bar{b}_{\text{C}}{}^{2}a_{\text{C}_{\text{MC}}\text{C}_{\text{MG}}}(Q) + \bar{b}_{\text{C}}\bar{b}_{\text{D}}a_{\text{C}_{\text{MC}}\text{H}_{\text{MG}}}(Q) + \bar{b}_{\text{H}}\bar{b}_{\text{D}}a_{\text{H}_{\text{MC}}\text{H}_{\text{MG}}}(Q) + \bar{b}_{\text{H}}\bar{b}_{\text{C}}a_{\text{H}_{\text{MC}}\text{C}_{\text{MG}}}(Q) \quad (10)$$

We note that while deuterium has a similar positive scattering length as carbon, hydrogen displays a negative scattering length of a magnitude of 55% of that of carbon (see Table 2). Hydrogenation of the different molecular units leads therefore to overall negative scattering length densities at the position of the methyl groups, while the CH_2 units end up at a very small negative scattering length density, and the carboxyl part of the side groups stays untouched. We will now discuss the resulting atom weighted partial structure factors yielding the experimentally observed structure factors.

1. PMMA-h8 (Figure 4a). At a first glance the scattering length weighted partial structure factors appear to show a completely different picture than those presented in Figure 3. There the MC/MC correlation function and the MC/SG counterpart were dominating. Here the MC/MC correlation (blue curve) is strongly reduced, reflecting the very weak average scattering length density of the main chain, where one carbon is basically compensated by the two negative hydrogens. Nevertheless, the peak structure at the interchain distance is still visible. The most amazing change occurs for the MC/SG correlation. On the basis of equally weighted atoms this function shows a strong negative peak around $Q = 0.70$ Å^{-1} (Figure 3). Now the sign of the peak is inverted, and the peak strength is significantly reduced. Changing the sign of the peak must mean that in this Q-regime the negative overall scattering length of the ester CH_3 group dominates the correlation function, telling us that the negative MC/SG correlation function comes from the out-of-phase correlation between the main chain and the ester methyl group.

To dwell further on this conclusion, we have inspected the simulation results in detailing the grouping of atoms. Figure 5 displays the MC/SG correlation function as discussed above, and in addition the correlation between the main chain and the ester CH_3 group as well as the main-chain/COO correlation function. This further subdivision supports strongly the above conclusions. The anticorrelation of the main chain and the ester methyl group is even more strongly pronounced than that of the total MC/SG correlation function. The strong negative peak around $Q = 0.70$ Å^{-1} shows the out-of-phase correlation between these two entities. The correlation between the main chain and the COO group is much weaker in this Q-regime.

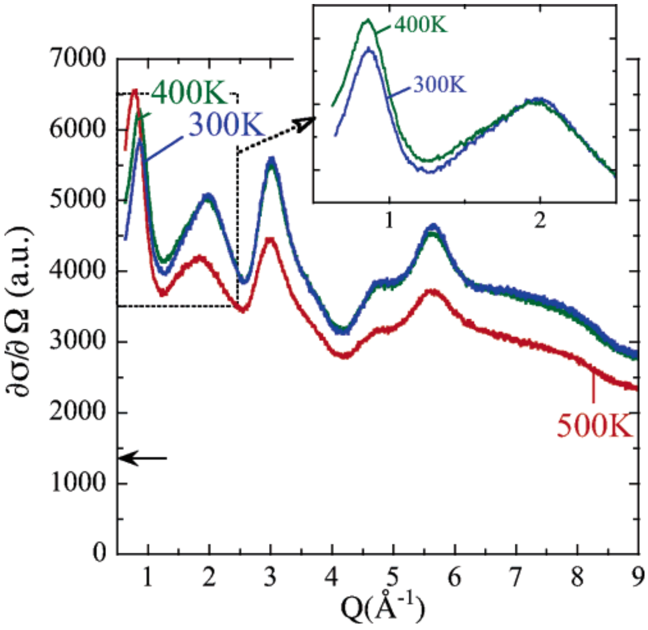

Figure 2. Total differential cross section determined by D20 for the fully deuterated sample PMMA-d8 at the three temperatures investigated. The horizontal arrow points the incoherent level estimated from the comparison with the DNS measurements at 300 K. In the inset the low-Q region has been blown up for the two lowest temperatures.

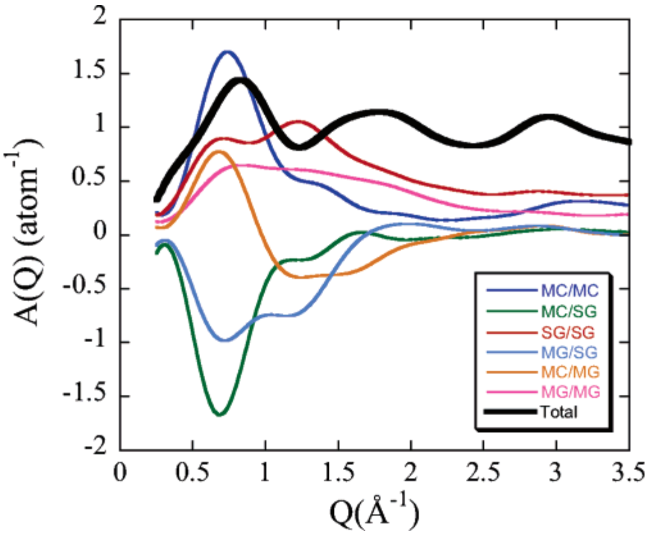

Figure 3. Fourier transform of the different partial radial distribution functions corresponding to the different atomic correlations within the molecular groups considered.

Similarly, the SG/SG correlation function, which displays a pronounced double-peak structure when it is atom weighted (see Figure 3), is now reduced to the second peak at $Q = 1.28$ Å^{-1}. We note that it is also reduced in weight by a factor of 2. Having hydrogenated methyl groups reduces the overall scattering length of this group significantly. Obviously, the relatively weak and

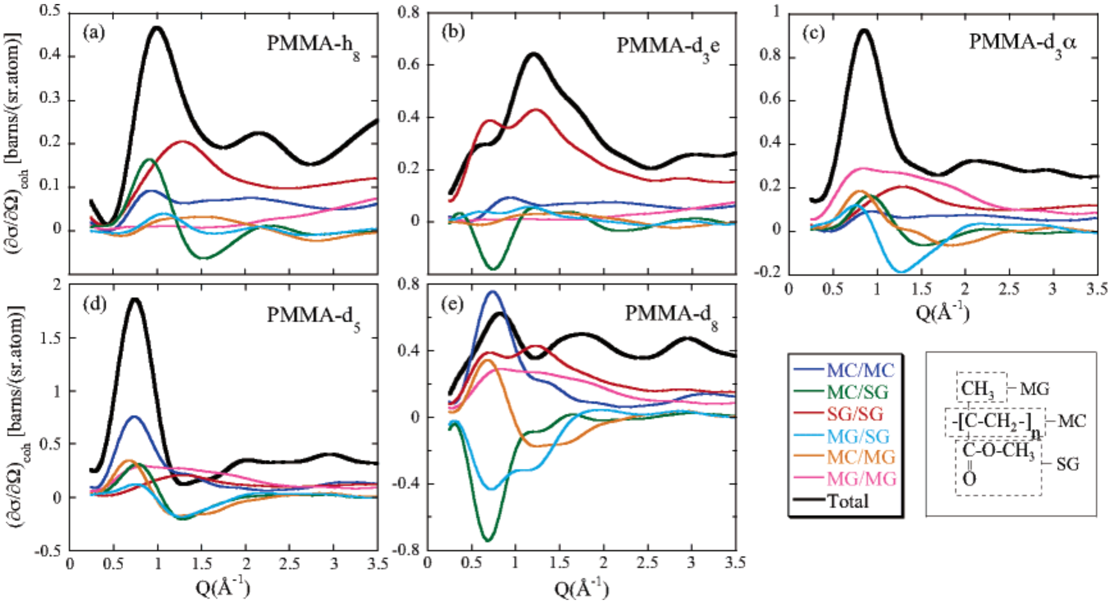

Figure 4. Coherent scattering calculated from the MD simulations for the different samples investigated. The contributions coming from the different molecular groups correlations, properly weighted by the corresponding neutron scattering lengths, are shown.

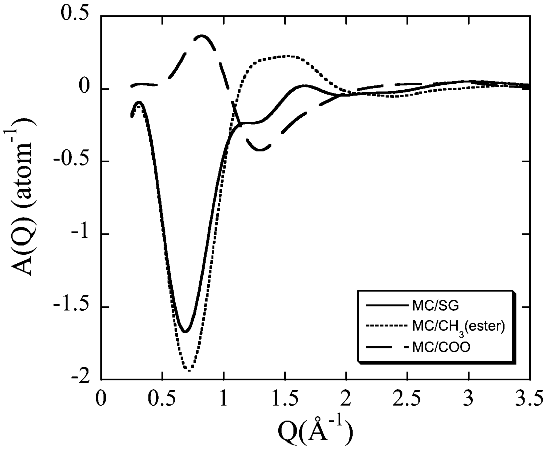

Figure 5. Contributions to the MC/SG correlation function: those relating MC and ester methyl group and those involving MC and carboxyl group (COO).

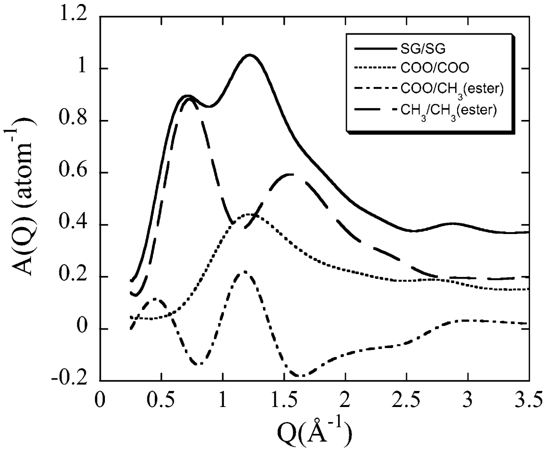

Figure 6. Contributions to the SG/SG correlation function: those relating only carboxyl groups, only ester methyl groups, and cross-terms involving carboxyl groups and ester methyl groups.

slightly negative outer part of the COO group, the CH_3 group correlation, and the corresponding cross term, contribute in the lower Q part of this correlation function, while the stronger carboxyl part contributions may be found in the second peak. Therefore, we assign this peak to the nearest-neighbor COO/COO group correlation along a given chain, while the missing low-Q part could relate to the nearest-neighbor intrachain CH_3 group correlation of oppositely arranged side groups corresponding to an estimated distance of 8.2 Å (we will come back to this point in section V.C.3). Figure 6 displays this conclusion also from the point of view of the simulation. Here, we have visualized the partial correlation functions within the SG/SG correlations. Thus, we have plotted the total CH_3/CH_3 correlation, the total COO/COO correlation, and the cross-term between the two for the atoms within the side group. The total correlation function is also shown. This separation in further subunits clearly shows that (i) the first peak within the side group/side group correlation functions comes from the correlations between the ester methyl group. (ii) The COO/COO correlations, on the other hand, display a peak around $Q = 1.2$ Å^{-1} at the position of the second peak of the total SG/SG correlation function as discussed before. (iii) The flank at $Q \approx 1.75$ Å^{-1} finally relates to ester methyl group/ester methyl group correlations, now at closest approach.

2. PMMA-d3e (Ester Methyl) (Figure 4b). Figure 4b displays the situation for a protonated chain, where the ester methyl group is deuterated. Here the structure factor is dominated by the SG/SG correlation function. With a deuterium-labeled ester methyl group the cross-correlations involving main chain and side groups become again negative, underlining the discussions above. This anticorrelation of main chain and ester methyl group diminishes the first peak of the structure factor compared to the SG/SG correlation function alone. Furthermore, there is the same MC/MC correlation contribution as in Figure 4a which, however, is already very weak compared to the two main contributions. All other correlation functions are negligible in the interesting lower-Q regime. Again we emphasize that the high-Q peak at $Q = 3$ Å^{-1} has no real counterpart in the different molecularly defined correlation functions and occurs as a sum of little structured contributions.

3. PMMA-d3α (α-Methyl Group) (Figure 4c). As expected with this labeling, the MG/MG correlation stands out, forming a broad peak in the lower-Q regime (as in the atom−atom correlations, see Figure 3). Nevertheless, the dominant feature of the experimental structure factor is a strong peak around $Q = 0.85$ Å^{-1} which comes about by a superposition of many small positive contributions. The most noteworthy is the MG/SG correlation which showed a strong negative double peak in Figure 3. The lower part now changes sign as the result of the negatively labeled ester methyl group. Its second peak ($Q = 1.26$ Å^{-1}), however, remains negative and appears to be part of the strong anticorrelations discussed above.

4. PMMA-d5 (Figure 4d). In this case the main chain as well as the α-methyl group is deuterated. The structure factor excels with a very strong peak at $Q = 0.81$ Å^{-1}, corresponding to the interchain correlation. An inspection of the different partial structure functions shows that this very strong peak comes from a positive superposition of contributions from most of the different partial structure functions discussed before. First, the MC/MC contribution dominates due to the strong positive scattering lengths along the chain. Second, as a consequence of the negative scattering length at the ester methyl group, the MC/SG correlation function becomes positive and adds constructively. Similarly, the MG/MG correlation function and the MG/MC correlation functions all add up with a positive contribution. Thus, this particular labeling emphasizes more strongly the overall periodicity of the structure. The first minimum at $Q = 1.3$ Å^{-1} is mainly coming from the negative contributions of the MC/SG, the MG/SG, and the MG/MC correlation functions. To a large extent these are again resulting from the anticorrelations discussed above. At higher Q the negatively labeled ester methyl group is only contributing weakly (see also Figure 5). Finally, the weak structure factor peaks at 2 and 3 Å^{-1} again are part of a complicated superposition of relatively unstructured partial correlation functions and do not directly reveal any special structural feature in the PMMA chain.

5. PMMA-d8 (Figure 4e). The structure factor built from a fully deuterated PMMA chain resembles closely the true structure factor as discussed at the beginning. In the case of a full deuteration all the carbons and deuteriums have the same scattering length, and also oxygen has only a slightly smaller scattering length than the other two. Thus, all contributions add up in a nearly identical fashion as in the case of the true structure factor discussed before.

C. Distribution Functions in Real Space: Intra- and Interchain Contributions. The amorphous cell for the simulations was constructed from four chains facilitating an evaluation of the distribution functions in terms of inter- and intrachain contributions. In the following we will discuss for some key atoms the contribution from the intra- and interchain correlations to the overall distribution function and relate the results to the previously discussed structure factors. The interchain contributions have been obtained by considering correlations among atoms of different chains in eq 6, while the intrachain contributions arise from atoms belonging to the same chain.

1. Main-Chain Correlations. We commence with the main chain. Figure 7a presents the intra- and interchain contributions to the radial correlation function $g_{C_{MC}C_{MC}}(r)$ of the main-chain carbon atoms. The red line displays the radial distribution function for main-chain carbon atoms of different chains—the inter contribution. This correlation function shows a relatively broad peak at about 9 Å, which is characteristic for an amorphous structure with a broad distribution of interchain distances. The peak position roughly corresponds to the average interchain distance (8.6 Å) estimated from the main peak of the MC/MC correlations in the Q-space (see Figure 3) by means of the Bragg approximation. However, we note that the shoulder in the MC/MC correlation function at $Q = 1.3$ Å^{-1} corresponding to a Bragg distance of 4.8 Å is not reflected in the interchain correlation.

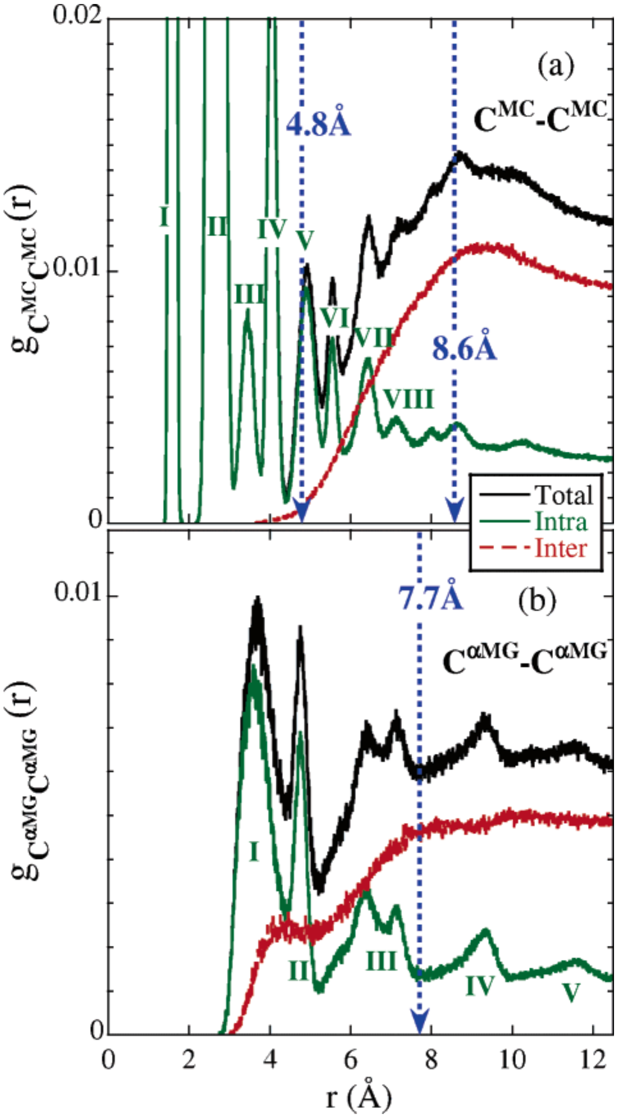

Figure 7. Radial probability distribution functions involving the carbons in the main chain (a) and in the α-methyl groups (b). The green curves have been calculated considering atoms within the same chain (intrachain correlations), while the red ones correspond to atoms belonging to different chains (interchain correlations). The black curves display the sum of both. The dotted vertical arrows show for comparison the average distances estimated from the main peaks of the MC/MC correlations (a) and MG/MG correlations (b) in the Q-space (Figure 3) by the Bragg approximation.

We now turn to the intrachain contributions that display a sequence of well-defined peaks up to distances of about 10 Å. Commencing with the peaks at short distances, the first (I) and second (II) peaks relate to the covalently bonded first and second carbon neighbors. The apparently broader second peak is in fact a double peak resulting from the two different bond angles along the chain (≈110° and ≈128°).[12] The peaks reflecting the third (III, IV) and fourth neighbors (V,VI) are also very well developed and are split into two components each. Peak III at $r = 3.4$ Å reflects the position of the third neighbor in the trans–gauche (t,g) conformation while peak IV arises from the corresponding all-trans state (t,t). We note that we observe strong deviations (up to 30°) from the ideal dihedral angle of 180° for a trans conformation. From the peak areas the probabilities for the two conformations may be evaluated. They are 73% for trans and 27% for gauche. Peak V is mainly related to the fourth neighbor in all-trans conformation; from the area a probability of about 40% evolves which relates well to the expectation for this state $(0.73)^3 = 39\%$. While peak VI probably stems from a combination of various (t,g) states, peak VII again mainly marks an all-trans conformation, now for a sequence of five carbons. This contribution amounts to about 2/3 of peak VII.

There exist also peaks corresponding to even larger distances beyond the fifth neighbor, but their intensities are much weaker—their positions could relate to several different combinations of trans−gauche states and cannot easily be assigned. From the dominance of the correlation peaks reflecting all-trans conformations it may be concluded that the chain locally is relatively stiff, which is also reflected in the large values reported for the characteristic ratio for this chain. In the literature values in the range $C_\infty = 7-9$ can be found for PMMA (see refs 12, 38, 39 and references therein).

The superposition of the intra- and intercorrelation is represented by the black curve in Figure 7a. This distribution function displays a broad peak at about 9 Å, reflecting the corresponding structure factor peak (Figure 3). It also shows several peaks in the region of 5 Å, i.e., in the range of the average Bragg distance corresponding to the shoulder around $Q = 1.3$ Å^{-1} in the partial structure factor (Figure 3). Thus, the main peak and the shoulder in the partial structure factor are of different origin: while the main peak is clearly a result of interchain correlations, the shoulder and also the higher Q oscillations are related to intrachain correlations.

2. α-Methyl Correlations. We now turn to the radial correlation function of the carbons in the α-methyl group $g_{\mathrm{C_{MG}C_{MG}}}(r)$. Figure 7b displays the corresponding intra- and interchain contributions. The interchain radial correlation function starts with a significant contribution around $r = 4$ Å and displays a weak peak around $r = 4.5$ Å. It raises further to larger distances reaching a plateau at about 8 Å. We note that the interchain correlation function has a first significant contribution in the same region where the intrachain contribution has its first double maximum. This phenomenon is quite different to the observations for the main chain, where the interchain correlation function is only important at larger distances around the average interchain distance. The first correlation distance of about 4.5 Å is very close to the van der Waals distance between methane (4.2 Å)[40] and shows that the α-methyl groups from two different chains are able to come very close. This may happen, e.g., by interdigitation of neighboring chains.

The intrachain pair distribution function again is characterized by a number of sharp peaks reaching toward long distances. The first double peak characterizes the conformational distances of first-neighbor α-methyl groups. Peak I at $r_{\mathrm{I}} = 3.63$ Å relates to the all-trans conformation while peak II ($r_{\mathrm{II}} = 4.76$ Å) reflects those corresponding to (t,g) and (g,g) states—these last in a strong minority, ≈4%. The fact that the all-trans state appears at a shorter distance than the (t,g) or (g,g) states even though the chain is syndiotactic is a consequence of the nonideal minima of the torsional potential. Beyond the first double peak a sequence of further rather well-defined higher-order peaks appear, which straightforwardly are related to the sequence of the higher neighbors. The double peak III relates to the second-nearest-neighbor α-methyl group with the first peak arising from the all-trans conformation or the sequence (t,t/g,g/t,t). The second peak contains (t/g,t,t,g/t) states. The peaks IV and V then identify third- and fourth-neighbor α-methyl groups. Again, the identifiable all-trans conformations are significantly more pronounced than peaks corresponding to states with gauche conformations, corroborating thereby the results already discussed in the context of the intrachain correlations of the main-chain carbons.

The black curve in Figure 7b represents the sum of the intra and inter contributions. This radial correlation function is still characterized by a number of pronounced peaks which are not reflected in the MG/MG structure factor in Figure 3. While the emerging low-Q peak in some way reflects the main interchain correlation, the pronounced peak structures in the carbon−carbon α-methyl group radial correlation functions appear to be masked by the disordered hydrogen atoms.

3. Side-Group Correlations. Figure 8 displays the radial correlation functions for the carbonyls, $g_{\mathrm{C_{COO}C_{COO}}}(r)$. We commence with the interchain correlation function which is characterized by a steep flank in the neighborhood of $r = 6$ Å, displaying a peak at about $r = 6.3$ Å followed by a plateau toward larger distances. Seemingly the carbonyls cannot approach each other as closely as the α-methyl group carbons. The sharp flank reflects to a certain extent the relatively strong local order inferred from the discussion of the MC/SG partial structure factor in the context of Figure 3.

The intrachain radial distribution function displays again a strong double peak with an intensity sequence now inverted compared to the corresponding α-methyl group function. Now the first peak is weaker than the second—the (t,t) conformations in this case belong to the larger distance $r_{\mathrm{II}} = 4.4$ Å. Beyond this initial doublet, higher-order peaks signify the second, third, and fourth neighboring carbonyls. Finally, the black curve gives the total correlation function. Comparing with Figure 6, where we have presented the different partial structure factors for the ester side group, we realize that at the average Bragg distance of 5.2 Å (corresponding to the peak position of the carboxyl partial structure factor) the radial correlation function in space of the carbonyl displays a minimum. Obviously, the COO/COO partial structure factor of Figure 6 must be very much influenced by the oxygen contributions.

Therefore, we have also studied the correlation function of the COO group as a whole (Figure 9a). Compared to Figure 8 we realize that the inclusion of the oxygen atoms changes the emerging correlation function significantly. First, at short distances the carbon−oxygen and oxygen−oxygen contributions appear as sharp lines, while the dominating doublet around 4 Å in Figure 8 is significantly broadened and shifted toward larger distances. Furthermore, the well-defined higher-order peaks in Figure 8 are strongly modified and blurred, giving raise to a shoulder in the region of the second-nearest neighbor and then only to very small modulations toward larger distances. Adding now the interchain correlation function (red line), we arrive at the black curve which displays a peak around 5.2 Å. By the Bragg approximation, this corresponds to $Q = 1.2$ Å^{-1}, where the partial correlation function in Figure 6 has its maximum.

Figure 9b investigates the correlations displayed by the ester methyl carbon atoms. Here both the interchain correlation function and the intrachain correlation function display strong first peaks at $r = 4.1$ Å, again corresponding to the van der Waals radius of a methyl group. Apparently, the ester methyl groups within one chain and those in between two different chains are able to approach each other equally well. While the intra peak at 4.1 Å corresponds to trans−gauche conformations of the main-chain carbons—in this case the syndiotactically related side groups are able to come close—the strong interchain

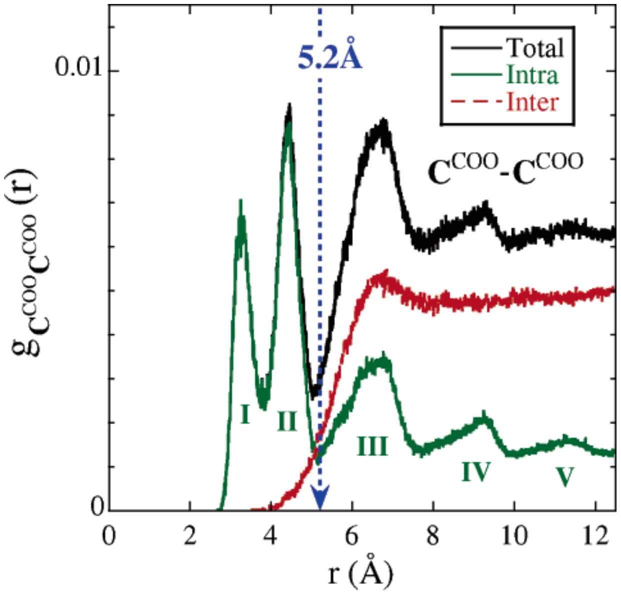

Figure 8. Radial probability distribution functions of the carbonyls (lines such as in Figure 7). The dotted vertical arrow indicates the average Bragg distance deduced from Figure 6.

peak at the same position corroborates the already stated interdigitation between chains and reflects the discussed strong local separation between side groups and backbones derived from the MC/SG partial structure factor of Figure 3. The second intramolecular peak at $r_{II} = 8$ Å encompasses on one hand contributions from syndiotactically attached ester groups at nearest-neighbor positions as well as contributions from main-chain gauche−gauche conformations. The total correlation function retains the double-peak structure which is very well reflected in the CH_3/CH_3 partial structure factor of Figure 6.

D. Comparison with Literature. As was commented on in the Introduction, most of the structural studies on PMMA have been performed by X-ray scattering. As far as we know, the only results reported on neutron diffraction in PMMA can be found in refs 13, 41, and 42. In ref 13, atactic PMMA samples with four different deuteration levels were measured without polarization analysis, and only the data corresponding to the fully deuterated sample were compared with simulation models optimized by the reverse Monte Carlo (RMC) method. The main focus was to improve the simulation method and to check the capability of the RMC procedure. The conclusions extracted concerning the structural features of atactic PMMA supported those previously pointed out on the basis of X-ray investigations.[9] To relate our results with those from earlier studies, we have calculated the X-ray diffraction intensity from our simulations. Thereby, we have used the Q-dependent atomic scattering factors for X-rays[43] instead of the scattering lengths for neutrons in the calculation of the structure factor. Figure 10 shows the computed X-ray scattering for PMMA. In Figure 10a it is compared with three different sets of literature data obtained by WAXS at room temperature. Taking into account the discrepancies that exist among the different experimental results, the corrections involved in the treatment of the X-rays measurements, as well as the differences in temperature, we can conclude that our simulation results are in quite reasonable agreement with the experimental curves. Thus, this comparison with the experimental data again validates the simulations. To dwell further in the X-rays analysis, we used the same grouping of the partial correlation functions, i.e., according to the molecular groups in the repeat unit, which are displayed in Figure 10b.

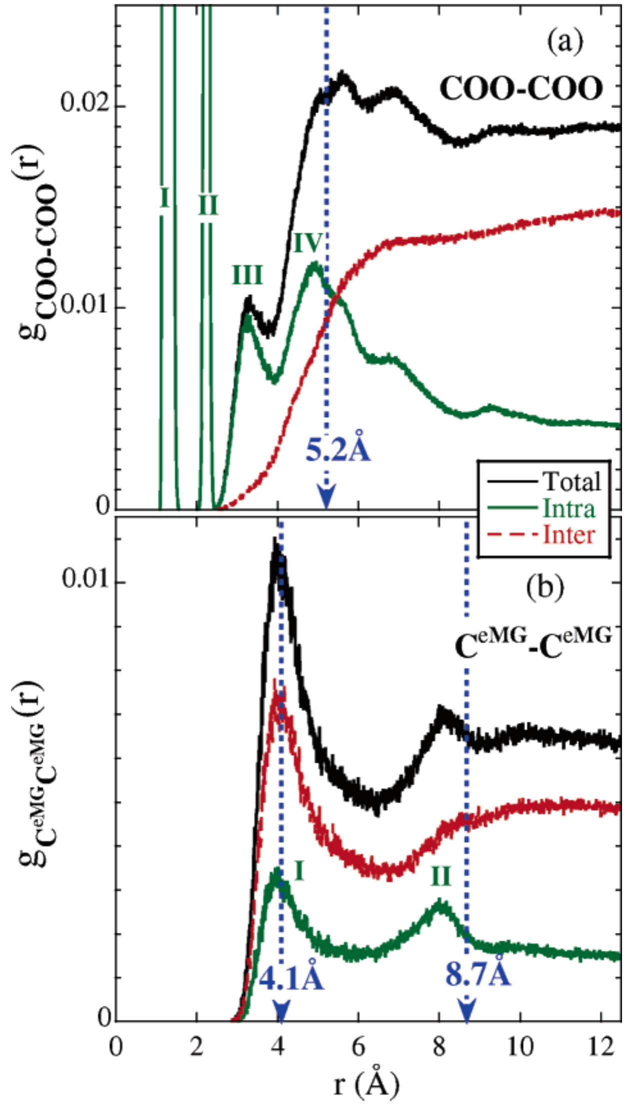

Figure 9. Radial probability distribution functions of the carboxyl group (COO) (a) and the ester methyl group carbons (b) (lines like in Figure 7). The dotted vertical arrows show the Bragg distances deduced from Figure 6.

An interesting conclusion derived from the literature is that the first (lowest-Q) peak in the WAXS pattern arises from both intra- and intermolecular components.[9] Our results indicate two main contributions to this peak: in the region of its low-Q flank (at $Q \approx 0.8$ Å^{-1}), we observe an influence from the MC/MC correlations, while at the high-Q flank (at $Q \approx 1.2$ Å^{-1}) the SG/SG correlations dominate (Figure 10b). Looking both at the MC/MC partial structure factor and the distribution function in real space for the main-chain carbon atoms, we found that the main-chain contribution to the first peak is mainly intermolecular. This is in good agreement with Lovell and Windle, who found the intermolecular component to the first peak at 0.95 Å^{-1}. Turning to the intramolecular contribution, it was observed by those authors at 1.2 Å^{-1}. The periodicity associated with this peak corresponds to the distance (5.2 Å) between two parallel lines, each one going through two consecutive ester groups. To compare with our results, we have displayed in Figure 10b the COO/COO correlation function, the maximum of which is located also at 1.2 Å^{-1}. This correlation indeed shows an important intramolecular contribution at the corresponding distance (Figure 9a).

Concerning the second and the third peaks in the X-ray pattern, Lovell and Windle proposed that they are intramolecular

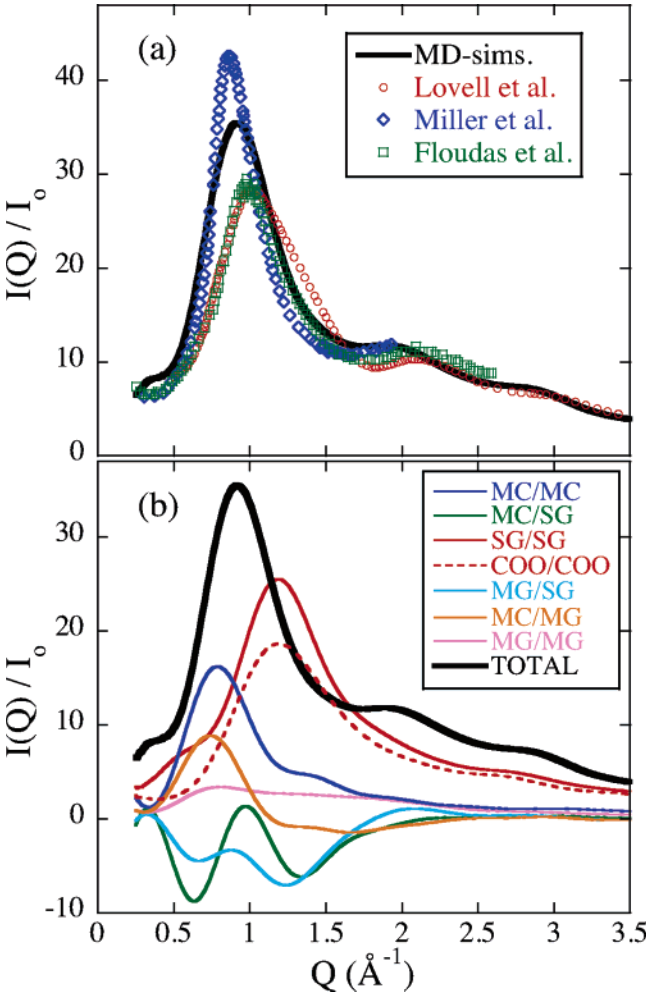

Figure 10. (a) Comparison between WAXS from PMMA as measured by Lovell and Windle,[9] Miller et al.,[7] and Floudas and Stepanek[6] and calculated from our simulations (solid black line). The experimental data have been multiplied by the corresponding factors to roughly coincide in the high-*Q* region. (b) Contributions to the X-ray structure factor from the different molecular groups correlations, as indicated in the inset.

in character, in agreement again with our results. Those authors related the second peak at about $Q = 2$ Å^{-1} with the repeat distance between the projection of two consecutive ester groups on the segment axis. From Figure 10b the X-rays second peak is clearly dominated by the SG/SG correlations or, more precisely, by the COO/COO correlation, and we know from Figure 9a that at this short distance the COO contribution is almost purely intramolecular arising from nearest-neighbor carboxyl groups. On the other hand, the authors assigned the third peak ($Q = 2.95$ Å^{-1}) to the repeat distance (2.15 Å) between one carbon and its second neighbor along the main chain (again projected on the segment axis). However, in Figure 10b we can see that the SG/SG correlation function is still largely dominant around the third maximum whereas the MC/MC correlation is quite weak. From our results the third peak seems to be related with the SG/SG and by extension to the COO/COO correlation that displays a purely intramolecular contribution at 2.24 Å (see Figure 9a).

A salient feature observed in this work is the anticorrelation between the main chain and the side group at the chain/chain repeat distance. This can be seen again in Figure 10b. It is clear that the PMMA melt displays a strong local ordering. In addition, the detailed investigation of the distribution functions in real space for both the ester- and the α-methyl groups suggests an interdigitation between the neighboring chains in PMMA. This observation reminds on the proposed nanophase separation in the higher P-*n*MA's where X-ray data were interpreted in this direction.[2,8] However, it has to be noted that, as far as we know, this was never discussed for PMMA. To support the strong local order and the interdigitation that we observe in PMMA, we may also comment that the interdigitation between the alkyl side chains reported in the poly(di-*n*-alkyl itaconate) series extends to the PMMA analogue, the poly(dimethyl itaconate), where the corresponding low-*Q* peak is already well developed.[10] By using the idealized model proposed by Arrighi et al.[10] with the WAXS data compiled by Beiner,[2] the expected value in PMMA for the typical distance between backbones would be of 9.2 ± 1.1 Å. This prediction is in good agreement with our results shown in Figure 7a. There it can be seen that the intermolecular contribution to the radial distribution function shows a peak at about 9 Å.

At this point, we may comment further on the recent work by Wind et al.[8] For P-*n*MA's with $N \geq 2$ a layered structure was proposed, the signature of which would be the X-ray peak at about 1.3 Å^{-1}, labeled as peak I as it was mentioned in the Introduction. Let us remember that P-*n*MA's show two other X-rays peaks which were labeled as peak II ($Q \approx 0.8$ Å^{-1}), related to intramolecular length scales, and peak III at lower *Q*'s, interpreted as the signature of some nanophase separation. For PMMA, a single low-*Q* peak at an intermediate position between peaks II and I is found by WAXS, which has been attributed to the merging of peak II and peak I by Wind et al.[8] However, we would rather suggest the label III/II for this peak. After our previous discussion it becomes evident that it comprises aspects from peak III—attributable to some nanophase separation—and peak II—characteristic for intramolecular correlations. These contributions are not resolved in the WAXS curve (see Figure 10b). We also note that the expected position for the so-called peak III in PMMA would be at lower *Q* than it is found experimentally.[7] A final comment relates to the possible layered structure in PMMA. Wind et al. did not find any indication for such feature in PMMA. In agreement with them, no signature of it is revealed by our results. At $d \approx 5$ Å, where the typical intermolecular distance for this layered structure should be found, we do not observe any significant intermolecular MC/MC contribution (see Figure 7a).

Finally, in accord with several authors,[9,12,44−46] we found that the syndiotactic PMMA chains exhibit a predominantly trans conformation. Lovell and Windle reported that the regular conformation in PMMA extends over a mean length of 16−20 backbone bonds. By computing the intensity of radiation in PMMA, Yoon and Flory[44,45] concluded that (t,t) conformations are maintained until an average length of about 9 units. From our simulations, we find portions as long as containing 14 backbone angles persisting in the all-trans conformation in PMMA. All these results emphasize that the syndiotactic PMMA chains have a strong preference for the trans conformation, leading to the conclusion that they are locally relatively stiff.

VI. Summary and Conclusions

In this work we have undertaken a combined neutron scattering and molecular dynamics simulation study on the local structure of syndiotactic PMMA in the amorphous state. Employing partial deuteration altogether five different partial structure factors have been investigated by neutron polarization analysis. Thereby, it became possible to extract quantitatively the coherent contribution to the total scattering. The different partial structures factors arose from deuterating different parts of the PMMA monomer. They show qualitatively different features with respect to peak positions and heights. The MD simulations in principle can be analyzed in terms of 45 different partial correlation functions. To gain better insight, they were grouped in terms of molecular substructures such as the main chain, the α-methyl group, and the ester side group. In this way six partial structure functions were evaluated and compared with the experiments, achieving overall good agreement. Furthermore, a real-space evaluation of characteristic radial distribution functions was undertaken in order to separate intra- and interchain contributions to the total correlation functions.

The following results stand out:

- PMMA exhibits a strong local order with an average main-chain distance of 8.6 Å. This value is somewhat larger than what is revealed from X-ray scattering, where intrachain correlations between the COO groups strongly affect the diffraction pattern.
- There is a strong anticorrelation between the main chain and the ester side groups hinting a precursor effect of the nanophase separation between side groups and main chain proposed for metacrylates which larger side groups.
- The amorphous structure is characterized by one average main-chain distance and does not reveal any precursor effect of a layered structure as proposed for higher P-*n*MA's.
- The real-space analysis showed a persisting close to all-trans structure of the main chain, corroborating thereby the large values for the characteristic ratio reported in the literature.
- The ester side groups, in particular the ester methyl groups, of different chains appear to be interdigitated, a statement which is also supported by the interchain correlation function of the α-methyl groups. This interdigitation is a second manifestation of the strong separation between the main-chain and the side-group spatial arrangements.

In conclusion, the combination of MD simulations and the measurement of different partial structure factors using neutron polarization analysis has allowed unravelling deep structural details of syndiotactic PMMA which were not available so far. In the future it will be important to extend such investigations also to higher order P-*n*MA's to solve the question of nanophase separation, which is still discussed controversially in the literature.

Acknowledgment. We thank the Institut Laue-Langevin (ILL, Grenoble, France) for experimental facilities and in particular Dr. Hansen for experimental support during diffraction experiments. We also thank I. Quintana for his help during the DNS measurements. This research project has been supported by the European Commission NoE SoftComp, Contract NMP3-CT-2004-502235. A.A., F.A., and J.C. acknowledge support from the projects MAT2004-01017 and 9/UPV00206.215-13568/2001. "Donostia International Physics Center" is also acknowledged. The European Commission, NMI3 Contract RII3-CT-2003-505925, supported the experiments at the Forschungsreaktor in Jülich.

References and Notes

(1) Beiner, M.; Schröter, K.; Hempel, E.; Reissig, S.; Donth, E. *Macromolecules* **1999**, *32*, 6278.
(2) Beiner, M. *Macromol. Rapid Commun.* **2001**, *22*, 869.
(3) Beiner, M.; Kabisch, O.; Reichl, S.; Huth, H. *J. Non-Cryst. Solids* **2002**, *307*, 658.
(4) Beiner, M.; Huth, H. *Nat. Mater.* **2003**, *2*, 595.
(5) Hiller, S.; Pascui, O.; Kabisch, O.; Reichert, D.; Beiner, M. *New J. Phys.* **2004**, *6*, 1.
(6) Floudas, G.; Stepanek, P. *Macromolecules* **1998**, *31*, 6951.
(7) Miller, R. L.; Boyer, R. F.; Heijboer, J. *J. Polym. Sci., Polym. Phys. Ed.* **1984**, *22*, 2021.
(8) Wind, M.; Graf, R.; Renker, S.; Spiess, H. W.; Steffen, W. *J. Chem. Phys.* **2005**, *117*, 6289.
(9) Lovell, R.; Windle, A. H. *Polymer* **1981**, *22*, 175.
(10) Arrighi, V.; Triolo, A.; McEwen, I. J.; Holmes, P. F.; Triolo, R.; Amenitsch, H. *Macromolecules* **2000**, *33*, 4989.
(11) Yamaguchi, S.; Hayashi, H.; Hamada, F.; Nakajima, A. *Macromolecules* **1984**, *17*, 2131.
(12) Sundarajan, P. R.; Flory, P. J. *J. Am. Chem. Soc.* **1974**, *96*, 5025.
(13) Ward, D. J.; Mitchell, G. R. *Phys. Scr.* **1995**, *T57*, 153.
(14) Eilhard, J.; Zirkel, A.; Tschöp, W.; Hahn, O.; Kremer, K.; Schärpf, O.; Richter, D.; Buchenau, U. *J. Chem. Phys.* **1999**, *110*, 1819.
(15) Furuya, H.; Mondello, M.; Yang, H.-J.; Roe, R.-J.; Erwin, R. W.; Han, C. C.; Smith, S. D. *Macromolecules* **1994**, *27*, 5674.
(16) Alvarez, F.; Colmenero, J.; Zorn, R.; Willner, L.; Richter, D. *Macromolecules* **2003**, *36*, 238.
(17) Iradi, I.; Alvarez, F.; Colmenero, J.; Arbe, A. *Physica B* **2004**, *350*, e881.
(18) Narros, A.; Arbe, A.; Alvarez, F.; Colmenero, J.; Zorn, R.; Schweika, W.; Richter, D. *Macromolecules* **2005**, *38*, 9847.
(19) Arbe, A.; Richter, D.; Colmenero, J.; Farago, B. *Phys. Rev. E* **1996**, *54*, 3853.
(20) Frick, B.; Richter, D.; Ritter, Cl. *Europhys. Lett.* **1989**, *9*, 557.
(21) Bedrov, D.; Smith, G. D.; Paul, W. *Phys. Rev. E* **2004**, *70*, 011804.
(22) Tsolou, G.; Mavrantzas, V. G.; Theodorou, D. N. *Macromolecules* **2005**, *38*, 1478.
(23) Hutnik, M.; Gentile, F. T.; Ludovice, P. J.; Suter, U. W.; Argon, A. S. *Macromolecules* **1991**, *24*, 5962.
(24) Han, J.; Boyd, R. H. *Polymer* **1996**, *37*, 1797.
(25) Ayyagari, C.; Bedrov, D.; Smith, G. D. *Macromolecules* **2000**, *33*, 6194.
(26) Lovesey, S. W. *Theory of Neutron Scattering from Condensed Matter*; Clarendon Press: Oxford, 1984.
(27) Squires, G. L. *Introduction to the Theory of Thermal Neutron Scattering*; Dover Publication Inc.: New York, 1996.
(28) http://www.fz-juelich.de/iff/wns/.
(29) Sun, H. *Macromolecules* **1995**, *28*, 701.
(30) Sun, H.; Mumby, S. J.; Maple, J. R.; Hagler, A. T. *J. Phys. Chem.* **1995**, *99*, 5873.
(31) Sun, H. *J. Phys. Chem. B* **1998**, *102*, 7338.
(32) Theodorou, D. N.; Suter, U. W. *Macromolecules* **1986**, *19*, 139.
(33) Theodorou, D. N.; Suter, U. W. *Macromolecules* **1986**, *19*, 379.
(34) Colmenero, J.; Alvarez, F.; Arbe, A. *Phys. Rev. E* **2002**, *65*, 041804.
(35) Genix, A.-C.; Arbe, A.; Alvarez, F.; Colmenero, J.; Willner, L.; Richter, D. *Phys. Rev. E* **2005**, *72*, 031808.
(36) Placzek, G. *Phys. Rev.* **1952**, *86*, 377.
(37) Yarnell, J. L.; Katz, M. J.; Wenzel, R. G.; Koenig, S. H. *Phys. Rev. A* **1974**, *7*, 2130.
(38) Subramanian, V.; Asirvatham, P. S.; Balakrishnan, R.; Ramasami, T. *Chem. Phys. Lett.* **2001**, *342*, 603.
(39) Fetters, L. J.; Lohse, D. J.; Richter, D.; Witten, T. A.; Zirkel, A. *Macromolecules* **1994**, *27*, 4639.
(40) Press, W. *J. Chem. Phys.* **1972**, *56*, 2597.
(41) Gabrys, B.; Higgins, J. S.; Schärpf, O. *J. Chem. Soc., Faraday Trans. 1* **1986**, *82*, 1923.
(42) Gabrys, B.; Higgins, J. S.; Schärpf, O. *J. Chem. Soc., Faraday Trans. 1* **1986**, *82*, 1929.
(43) *International Tables for X-ray Crystallography*; The Kynoch Press: Birmingham, England, 1974; Vol. IV, p 99.
(44) Yoon, D. Y.; Flory, P. J. *Polymer* **1975**, *16*, 645.
(45) Yoon, D. Y.; Flory, P. J. *Macromolecules* **1976**, *9*, 299.
(46) Vacatello, M.; Flory, P. J. *Macromolecules* **1986**, *19*, 405.

MA060370T